International Journal of Fatigue 185 (2024) 108365

Contents lists available at ScienceDirect

International Journal of Fatigue

journal homepage: www.elsevier.com/locate/ijfatigue

Investigating post-processing impact on fatigue performance of LPBF Ti6Al4V with heat treatment, high pressure heat treatment, and dry electropolishing strategies

Omar Bologna [a,*], Silvia Cecchel [b], Giovanna Cornacchia [a], Andrea Avanzini [a], Raffaele Sepe [c], Filippo Berto [d], Nima Razavi [e]

[a] Department of Mechanical and Industrial Engineering, University of Brescia, via Branze 38, 25123 Brescia, Italy
[b] Streparava SpA, Via Zocco 13, 25030 Adro, BS, Italy
[c] Department of Industrial Engineering, University of Salerno, via Giovanni Paolo II, 132 Fisciano, SA, Italy
[d] Department of Chemical Engineering, Materials and Environment, Sapienza University of Rome, Rome, Italy
[e] Department of Mechanical and Industrial Engineering, Norwegian University of Science and Technology (NTNU), Trondheim, Norway

ARTICLE INFO

Keywords:
Laser powder bed fusion
Fatigue
Post-processing
High pressure heat treatment
Dry electropolishing

ABSTRACT

This study investigates the impact of post-processing techniques on the fatigue behaviour of specimens in Ti6Al4V made by laser powder bed fusion (LPBF) for relevant applications, such as motorsport. Despite the LPBF advantages in terms of complex design and weight reduction, challenges such as reduced fatigue performance persist. Therefore, the application of post-processing treatments can play a critical role. In addition to traditional sandblasting (SB), three post-processing conditions were investigated to enhance mechanical properties under quasi-static and fatigue loading conditions: heat treatment (HT) and the innovative High Pressure Heat Treatment (HPHT) along with dry electropolishing (EP) treatment. The results indicate that both the HT and HPHT treatments produced a macrostructure with equiaxial grains composed of fine $\alpha + \beta$ lamellae. Mechanical analyses demonstrated that the HPHT-SB-EP condition exhibits properties comparable to those of forged Ti6Al4V used in the automotive field, with a good balance between strength and ductility. The EP treatment effectively reduced surface roughness and inherent surface irregularities caused by the LPBF process. The best fatigue results were achieved with the HPHT-SB-EP condition, despite data scattering. An increase in fatigue resistance was observed by using SB at a higher pressure.

1. Introduction

Laser powder bed fusion (LPBF) selectively fuses metal powder layers into desired 3D shapes using a laser source, offering advantages like shortened lead times, improved material efficiency, and the ability to create complex geometries not feasible with conventional manufacturing technologies [1,2]. LPBF's potential impact on the automotive and aerospace industries lies in enhancing vehicle performance and achieving weight reduction [3,4]. Even minor weight reductions significantly improve fuel efficiency and reduce emissions [5–7]. Nevertheless, challenges remain, including the generally reduced fatigue performance of LPBF-produced components compared to conventionally manufactured parts. This is attributed to inherent factors like defects, microstructural heterogeneities, surface roughness, and residual stresses in as-built LPBF metallic parts, leading to local fatigue failure [8–11]. In this respect, post-processing methods like heat treatment, surface treatment, and hot isostatic pressing (HIP) can be employed to mitigate challenges and optimize the mechanical properties of LPBF-produced components [12,13].

This study is part of a comprehensive research effort aimed at reducing the weight of a connecting rod (conrod) for the motorsport industry. The conrod is entirely constructed from LPBF Ti6Al4V alloy and features an innovative, non-conventional structural design [14] that can be manufactured efficiently by means of additive manufacturing technologies. The choice of Ti6Al4V alloy is driven by its high strength-to-density ratio and excellent corrosion resistance, despite its higher cost compared to traditional materials like steel [15–17]. In prior research, topological optimization was applied to a conventionally manufactured

* Corresponding author.
E-mail address: omar.bologna@unibs.it (O. Bologna).

https://doi.org/10.1016/j.ijfatigue.2024.108365
Received 26 February 2024; Received in revised form 22 April 2024; Accepted 29 April 2024
Available online 1 May 2024

conrod to achieve weight reduction and leverage the advantages of LPBF over traditional forging methods [14]. The result was a LPBF multi-branch structure, leading to a weight reduction of 45 % compared to steel and 15 % compared to titanium forging. Moreover, the LPBF process allows the conrod production in two separate parts, eliminating challenging machining operations and enabling the integration of conformed cooling channels [14]. To attain mechanical properties comparable to the wrought counterpart used in automotive applications, a post-processing treatment involving super-β-transus solubilization followed by tempering was selected for LPBF Ti6Al4V, following a dedicated experimental phase [18]. This treatment resulted in an isotropic macrostructure with thin $\alpha + \beta$ lamellae within equiaxial new β grains, characterized by low residual stresses and high corrosion resistance. Fatigue tests on full-scale prototypes also gave preliminary information [19], but further investigations on methods to improve fatigue resistance without machining operations are necessary to better assess the full potential for lightweighting of the proposed solution.

Several studies in the literature focus on the fatigue behaviour of LPBF Ti6Al4V with post-processing treatments [20–24]. Hybrid post-processing, involving tailored combination of thermal and surface treatments, is often employed. Bhandari & Gaur [22] investigated fatigue properties in different thermal and surface conditions for LPBF Ti6Al4V specimens. Findings indicated that sequential heat treatment, HIP and machining result in the most significant improvement of fatigue strength and ductility, even though at the expense of tensile strength with respect to the as-built state. Hills *et al.* [23] showed that chemically etched LPBF Ti6Al4V exhibits increased fatigue strength with longer etching times. The addition of HIP treatment further improved fatigue limits, making them comparable to those of wrought machined and polished counterparts. Emanuelli *et al.* [24] studied the fatigue strength of LPBF Ti6Al4V under compressive residual stresses induced by turning and post sub-β-transus heat treatment. The research revealed that temperature had a minimal impact on fatigue strength, with defects and residual stresses induced by turning being the primary influencing factors. The findings from Sun *et al.* [25] on electron powder bed fused Ti6Al4V Grade 23 concluded that a minimum fatigue limit of 220 MPa can be achieved by both HIP and appropriate surface treatments. General findings highlight the critical role of surface quality in LPBF parts. The inherent high surface roughness, attributed to the staircase effect, unmelted powder particles, and surface defects, are key considerations [1]. A rough surface significantly diminishes fatigue strength, with surface aberrations serving as prominent stress concentrators in high-stress regions [26,27]. The literature reports significant variability in fatigue performance, with a scatter in fatigue strength exceeding 400 MPa for a given number of cycles to failure across a substantial portion of the data set [28].This is due to a variety of factors, including the elevated number of process parameters and part geometry which can affect mechanical behaviour and influence the orientation, shape, and dimension of defects, especially in presence of acute angles and sudden shape changes. Notably, existing literature predominantly examines specimens subjected to mechanical machining, with limited and disparate information available for those undergoing various post-processing treatments, particularly for near-net-shape components. These components require surface post-processing techniques unrestricted by geometric limitations, to enhance fatigue behaviour, such as electropolishing [29].

Dry electropolishing is an innovative process that utilizes an ion transport mechanism through macroporous styrene–divinylbenzene copolymer particles that retain a trace amount of sulfonic acid, reducing surface roughness [30–32]. Characterized by the absence of induced residual stresses, minimal material removal, and applicability to complex-shaped parts, dry electropolishing offers advantages over traditional liquid electropolishing, including reduced chemical waste and more uniform polishing. To improve fatigue performance, reduce internal porosity, and maintain ductility in Ti6Al4V while preserving strength, it is usual to employ HIP followed by heat treatment, which typically involves a solution treatment and tempering [33,34]. However, this sequence may induce pore regrowth if argon, with low solubility in titanium alloys, is initially trapped within the powder. The pressure of this entrapped gas could increase during the HIP process, causing significant expansion in subsequent high temperature heat treatment [35,36]. An innovative process, named High Pressure Heat Treatment (HPHT), allows to perform the elimination of internal porosity and heat treatment at high cooling rates simultaneously. The possibility to perform rapid cooling and quenching directly in the HIP unit eliminates the need for additional machinery and subsequent heat treatment steps. HPHT primarily aims to reduce porosity content while preserving the desired microstructure and minimizing the overall cycle time [37,38]. During HPHT, in-situ heat treatment in the HIP system prevents pore regrowth issues normally associated to sequential HIP and heat treatment steps [39].

This paper investigates the impact of post-processing on fatigue behaviour of Ti6Al4V specimens fabricated via LPBF. The study explores various post-processing conditions, emphasizing the effects of heat treatment, HPHT, and dry electropolishing techniques on cyclic properties. Beyond fatigue testing, the research includes a comprehensive analysis of microstructures and mechanical properties. The results of this study can enhance understanding and consolidate knowledge regarding the impact of the studied post-processing techniques on the fatigue behaviour of LPBF Ti6Al4V components.

2. Materials and methods

2.1. Specimen preparation

Fatigue and tensile specimens were produced with Ti6Al4V commercial powder from EOS GmbH by a DMLS machine “EOSINT M290” system. The nominal composition of the powder, with a mean diameter of 50 μm, is reported in Table 1 [40]. The LPBF system operated under standard deposition parameters for the EOSINT M290 system in an argon atmosphere. All Specimens were vertically built (Z axis) on a Ti6Al4V alloy base plate (X-Y plane). To assess the real properties of additively manufactured component, the surface of the specimens obtained by LPBF was left in as built condition, and only the supporting structures, laying on the bottom end of the specimens, were mechanically removed before testing.

Regarding post-processing treatments, Table 2 illustrates the different conditions applied to the LPBF tensile and fatigue specimens. For the sake of clarity, the following acronyms are used: heat treatment (HT), High Pressure Heat Treatment (HPHT), sandblasting (SB), and dry electropolishing (EP). It is important to emphasize that in the acronym, the treatments performed are listed in chronological order. It is worth noting that after the two heat treatments (HT and HPHT) all specimens underwent blasting with zirconia beads (diameter 125–250 μm). This step was carried out to eliminate the oxide layer formed during the additive manufacturing process and to smooth the surface asperities. The parameters were chosen for maximum reliability in the context of an additive manufacturing automotive application.

In relation to this aspect, it is highlighted that the characterization of the specimens involved two testing campaigns. The first campaign considered specimens (1st series) where the specimens were blasted with a maximum pressure of 3 bar, and the second one (2nd series) where the specimens were blasted with a maximum pressure of 8 bar. The tensile specimens were blasted with the same parameters of the fatigue ones, obtaining the same average surface roughness (Ra) values. For each specimen, the Ra value was obtained as the average of three longitudinal measurements on one shoulder and three on the other by means of a TRIBOtechnic profilometer with a contact force of 5 mN and a tip radius of 5 μm. Three additional measurements were performed on the gauge length of each tensile specimen, with similar results. The average Ra values obtained are shown in Table 3.

Delving further into the details regarding the post-processing

Table 1
Nominal chemical composition (wt. %) of the commercial EOS powder.

	Al	V	O	N	C	H	Fe	Y	Ti
Ti6Al4V	6.75	4.50	0.20	0.05	0.08	0.015	0.30	0.005	Balance

Table 2
Specimens and treatments.

Treatments				
Specimens	Heat Treatment (HT)	High Pressure Heat Treatment (HPHT)	Sandblasting (SB)	Dry electropolishing (EP)
HT-SB	Yes	No	Yes	No
HT-SB-EP	Yes	No	Yes	Yes
HPHT-SB-EP	No	Yes	Yes	Yes

Table 3
Average surface roughness and maximum height of profile of 1st and 2nd series.

Specimen series	Specimen condition	Average surface roughness, Ra [μm]	Maximum height of roughness profile, Rt [μm]
1st series	HT-SB	5.6	27.4
	HT-SB-EP	3.3	13.9
	HPHT-SB-EP	3.3	13.9
2nd series	HT-SB	2.5	14.7
	HT-SB-EP	1.7	10.5
	HPHT-SB-EP	1.7	10.5

treatments, the chosen heat treatment (HT) emerges as the most favourable option, as detailed in a previous study by Cecchel *et al.* [18]. After several investigations, it is evident that HT exhibits superior overall results, manifesting relevant mechanical properties, elevated corrosion resistance, and almost negligible residual stresses. For additional details about these properties, including the methods adopted and the experimental results in all the conditions analysed, please refer to a specific previous research of some of the authors [18]. The equiaxed and isotropic macrostructure, coupled with the presence of a mixture of fine α lamellae and β phase, is expected to confer heightened resistance to fatigue stresses. This HT entails a super-β-transus solubilization at 1015 °C for 0.5 h with argon quenching, followed by tempering at 730 °C for 2 h. The HT is conducted under high vacuum (10^{-6} mbar) using a "TAV H3 all metal" furnace, with argon utilized for cooling (cooling rate ≈ 9 ℃/s) after both solution annealing and tempering.

In addition to verifying the fatigue properties of the heat treatment selected from previous research [18], a treatment involving pressure was introduced. This treatment is intended to enhance fatigue resistance by reducing eventual porosities and improving surface finish [23,25,41,42]. In particular, High Pressure Heat Treatment (HPHT) is applied using a "QIH 60" machine from Quintus Technologies. It follows the same time–temperature cycle as HT and includes a pressurization of 2000 bar.

For surface improvement, dry electropolishing (EP) is employed with a "DLyte PRO500" system from Gpa Innova with DLyte 01-S commercial medium.

2.2. Metallurgical characterization

For metallographic observations, specimens in the different conditions were sectioned transversely (*X-Y* plane) and longitudinally (*X-Z* plane) at the same location of the higher gripped end with respect to the build height and prepared with standard metallographic techniques (ground with a series of 80 – 4000 grit SiC paper and polished until 1 μm diamond paste). Finally, in order to better investigate microstructures, the samples were etched with a 10 ml H_2O + 5 ml HNO_3 + 1 ml HF solution according to ASTM E407 standard. The etched samples microstructure was examined using a Leica DMI 5000 M optical microscope (OM) and a LEO EVO-40 XVP scanning electron microscope (SEM).

2.3. Tensile and hardness test

Displacement-controlled tensile tests to assess Young's modulus (E), yield strength (σ_y), ultimate tensile strength (σ_R) and elongation at failure were performed at room temperature following UNI EN ISO 6892–1:2009 [43] on cylindrical specimens with a length of 60 mm, a gauge length of 20 mm, and a gauge diameter of 4 mm. An electromechanical testing machine Instron 3369 equipped with a 50 kN load cell at a displacement rate of 1 mm•min^{-1} was used. The strain was measured using a 12.5 mm extensometer. The stress is measured as the load divided by the measured cross-sectional area before the test. The tensile stress is measured as the applied load divided by the measured cross-sectional area of the specimen gauge-section before the test. A minimum of eight tensile specimens were tested for each post-processing condition.

Vickers microhardness measurements (HV) on the polished and etched surfaces from the *X-Y* plane of the higher gripped end with respect to the vertical build after post-processing treatments were conducted using a Mitutoyo HM-200 machine. This was aimed at observing the influence of microstructural changes induced by HT and HPHT. All tests were carried out under a 9.8 N (1 kgf) load applied for 15 s according to ASTM E92-16 [44]. Results are presented as measurements from edge to edge along three lines (see Fig. 5) with at least 15 indentations for each line.

2.4. Fatigue test

SEM micrographs were acquired from the gripped end of the specimens before fatigue tests to verify the surface quality.

Fatigue tests were carried out on an average of at least ten specimens (usually 12 with re-tested specimens) for smooth geometry (see Fig. 1). All tests have been carried out at room temperature under load control using a sinusoidal signal in uniaxial tension with a frequency $f = 20$ Hz and a load ratio $R = 0.01$, following ASTM E466-21 [45]. The failure criterion was the total failure of specimen, and the run-out limit was set equal to 2×10^6 cycles.

The maximum stress (σ_{max}) and the number of cycles at failure (N_f) collected from each test were subsequently related to survival probabilities (P_s) of 10 % (upper bound), 50 % (mean curve), and 90 % (lower bound) based on ASTM E739-10 [46] and BS ISO 12107:2003 [47] standards through statistical analysis. Following this procedure, the inverse slope factor ($k = 1/B$) and the scatter index (T_σ) (i.e. the ratio between the stress corresponding to 10 % and 90 % P_S) were identified for each *S-N* curve. During fatigue data analysis, stress values were corrected in terms of the cross-sectional area of the specimen gauge-section measured before the test.

The fracture surfaces of failed specimens were investigated by means of SEM analyses with a FEI QUANTA 650 FEG SEM and a LEO EVO-40 XVP SEM to evaluate the fatigue failure mechanisms. Upon SEM analyses, defects at the fatigue crack initiation were measured by considering the actual area of the defect size.

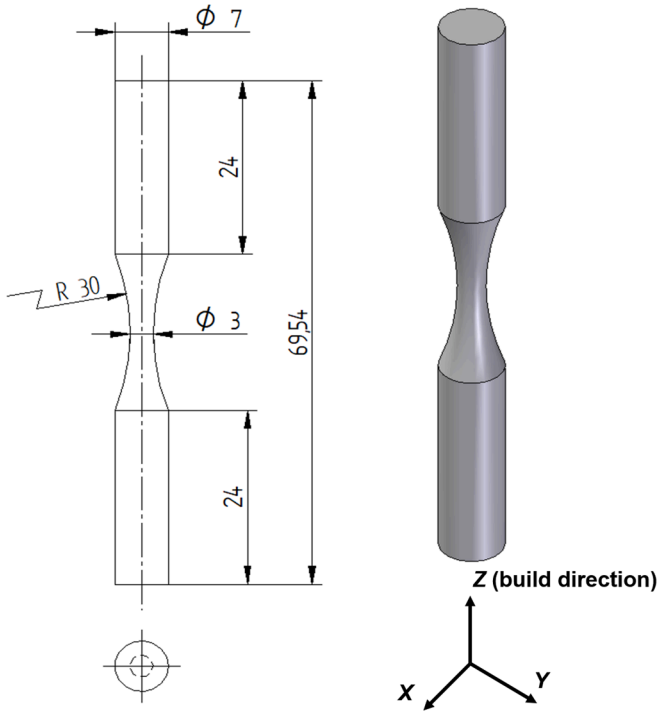

Fig. 1. Fatigue test specimen geometry and build direction (*Z* axis). Dimensions in mm.

3. Results and discussion

3.1. Metallurgical characterization

Fig. 2 shows optical micrographs of LPBF Ti6Al4V specimens at different magnifications for the *X-Y* plane and the *X-Z* plane of the vertical build (transversal and longitudinal directions respectively) in all conditions.

From a metallurgical standpoint, the initial noteworthy observation is that the micrographs obtained from the two HT and HPHT post-processing treatments exhibit a highly similar structure, revealing the presence of α (light) and β (dark) phases. In particular, the micrographs at lower magnifications in Fig. 2a, 2c, 2e, 2 g, 2i, and 2 k reveal isotropic macrostructures consisting of equiaxial parent β grains, resulting from quenching from the β field. Such microstructures confirm previous investigations and are in contrast with the anisotropic elongated previous β grains observed in the as-built condition [18]. The equiaxial β grains observed are related to the diffusionless transformation of the body-centered cubic (BCC) β phase into the hexagonal α' phase that is supposed to take place as a consequence of the rapid cooling after stationing in the β field during the solubilization treatment [18]. At higher magnifications, it is possible to observe inside the parent β grains, $\alpha + \beta$ phases, where α can be found both in form of lamellae arranged in colonies within the grains structure (see red arrows in Fig. 2d, 2f, and 2j) and basketweave (Widmänstatten) structure, and β is detected mainly as a line-shaped phase at the α plates boundary. Indeed, α plates forming triangular patterns typical of Widmänstatten structure can be appreciated in Fig. 2b, 2f, and 2j (highlighted with red triangles). These patterns are formed due to the Burger relationship between hexagonal closed-packed (HCP) α and BCC β phase, according to which there are twelve possible variants in the α plates orientation inside a parent β grain [20]. Furthermore, the presence of allotriomorph α phase at parent β grain boundaries is evident (indicated with yellow signs in Fig. 2d, 2f, and 2j), which often contributes to the formation of α colonies. This microstructure is developed through super-β-transus solubilization treatment followed by quenching, where acicular α' martensite is predicted due to the argon quenching from the β field. During the subsequent tempering treatment, the α' martensite is supposed to decompose into the stable $\alpha + \beta$ mixture [15,18,48,49]. Metallurgical characterization revealed no relevant defects such as porosities or internal lack of fusions (LOF) at all magnifications. Additionally, as expected, no discernible influence on the microstructure from the EP post-processing surface treatment was noted. It should be noted that the reported microstructures are representative of both the 1st and 2nd series of fatigue and tensile specimens, as no differences were observed upon analyses.

To provide a complementary perspective at higher magnifications, SEM images are presented in Fig. 3, where the α phase appears dark and the β phase appears light. These SEM micrographs validate the microstructure observed through OM analysis as described above, but α lamellae with different orientations are more distinctly visible. Measurements of both the α plate thickness and the volume fraction of the β phase were performed by some of the authors upon SEM analysis on LPBF Ti6Al4V specimens during previous works on the same LPBF built of production and heat treatment. Results indicated α lamellae with an average thickness t = 1192 ± 138 nm and β phase between 20 ± 3 % [18] and 22 ± 5 % volume fraction [50].

3.2. Tensile and hardness tests

Fig. 4 illustrates the stress–strain curves for each tested condition, and Table 4 presents the average of mechanical property values divided into 1st and 2nd series. It is pointed out that, for each condition, the decision was made to display the curve with the highest ultimate tensile strength. However, it is important to note that the observed trends were consistently very similar, with negligible variations in behaviours.

The initial observation is the alignment of tensile property values between the 1st and 2nd series, affirming the stability and precision of the LPBF process and the applied post-processing treatments. Subsequently, these data were compared with the tensile properties obtained from conventionally forged specimens manufactured with the same alloy. This comparative analysis refers to data reported in a prior study (see Cecchel *et al.* [14]: $E = 117 \pm 5$ GPa, $\sigma_y = 956 \pm 6$ MPa, $\sigma_R = 1034 \pm 5$ MPa, elongation at failure = 14 ± 1 %). Compared to their traditionally forged counterpart, only the HPHT-SB-EP specimens exhibit comparable properties. However, the values for the other two conditions do not differ significantly, especially considering the standard deviations. This finding is in agreement with the results from Plöcl *et al.* [51] regarding the use of a post-processing high pressure heat treatment in order to gain a good trade-off between strength and ductility of AM Ti6Al4V parts. Even though the static properties are not markedly influenced by the surface finish, when comparing HT-SB with HT-SB-EP, a slight improvement in yield strength and ultimate tensile strength due to polishing is noticeable. This trend is promising regarding the beneficial effect of EP on fatigue strength. On the other hand, when comparing the two different treatments with the same polishing EP (HT-SB-EP vs. HPHT-SB-EP), the effect of applied pressure is evident in terms of improvement in both ultimate tensile strength and yield strength. This phenomenon is likely attributed to the closure of any existing defect. A note should be made regarding the elongation at failure, as it appears to be the only data point that does not faithfully follow the trends outlined above. However, it is essential to emphasize that, considering the standard deviation, the values obtained in all three conditions for both the 1st and 2nd series are very close. In conclusion, it is possible to affirm that HPHT-SB-EP exhibits average values of σ_y, σ_R, and elongation at failure higher than the HT-SB-EP.

Fig. 5 shows the HV1 microhardness profiles of samples in all post-processing conditions (HT-SB, HT-SB-EP, and HPHT-SB-EP) for both the 1st and 2nd series along the *X-Y* plane. In particular, the graphs depict HV1 microhardness profiles on the cross-sectional areas obtained from the fatigue specimens of the 1st and 2nd series, aiming to assess the continuity of the specimens concerning their mechanical characteristics. Besides minor edge effects, some fluctuations were registered along the

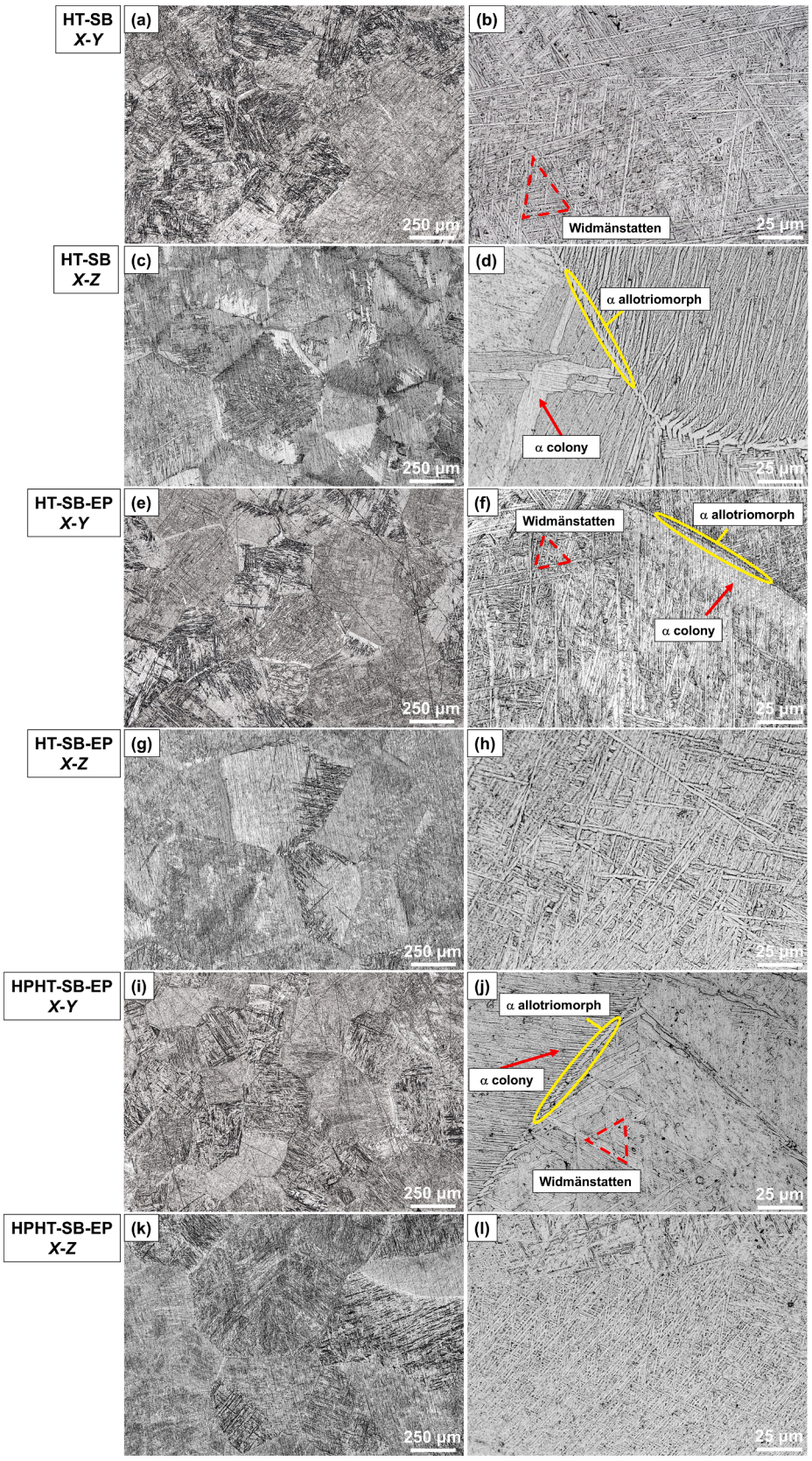

Fig. 2. Optical micrographs of LPBF Ti6Al4V specimens at different magnifications (a–d) HT-SB, (e–h) HT-SB-EP, and (i–l) HPHT-SB-EP. *X-Y* and *X-Z* planes refer to the coordinate system shown in Fig. 1. Red triangles highlight Widmänstatten patterns, red arrows indicate *α* colonies, and yellow signs point out α allotriomorphs.

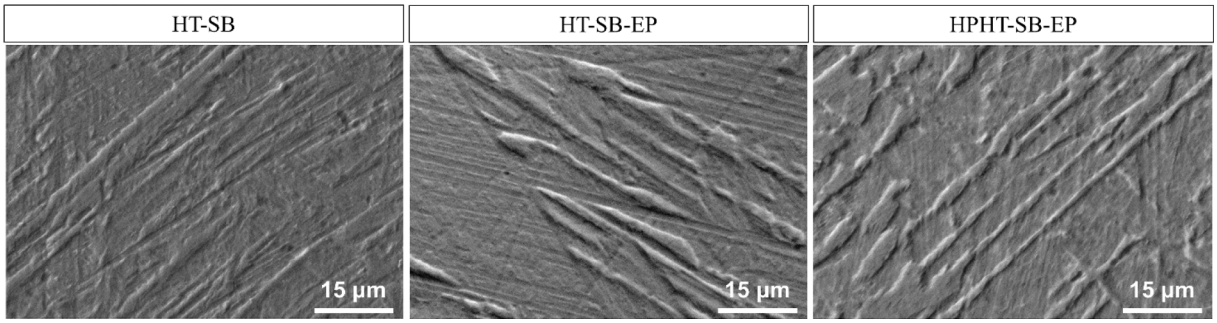

Fig. 3. SEM micrographs of LBPF Ti6Al4V specimen in HT-SB, HT-SB-EP, and HPHT-SB-EP conditions.

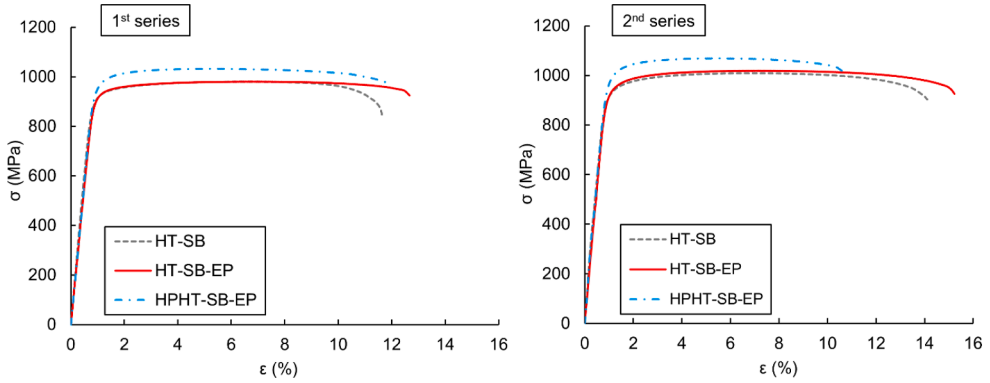

Fig. 4. Tensile curves for HT-SB, HT-SB-EP, and HPHT-SB-EP specimens of 1st series (left) and 2nd series (right).

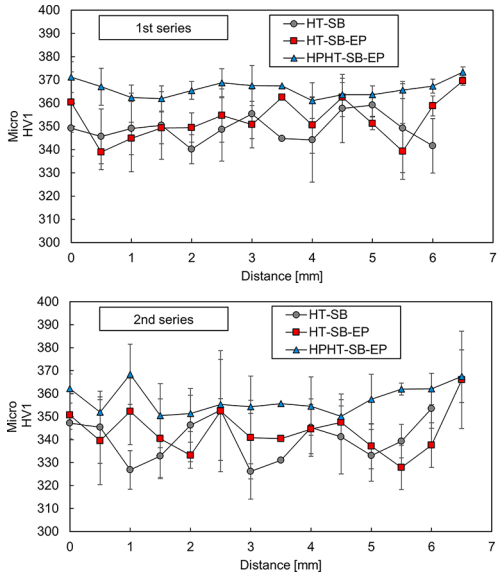

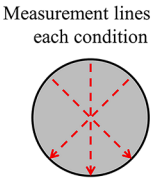

1st series conditions	HV1
HT-SB	349 ± 13
HT-SB-EP	353 ± 12
HPHT-SB-EP	366 ± 6
2nd series conditions	
HT-SB	342 ± 16
HT-SB-EP	344 ± 16
HPHT-SB-EP	357 ± 10

Fig. 5. Microhardness profiles of HT-SB, HT-SB-EP, and HPHT-SB-EP samples of 1st series (upper) and 2nd series (lower) with corresponding average HV1 values across the whole cross-section, and the three measurement lines from edge to edge.

profiles of the samples, possibly attributed to the presence of harder phases or potential defects for a given indented location[52,53]. The results indicate that the microhardness profile is very similar between the conditions, with slightly higher hardness values and less fluctuations for the HPHT-SB-EP condition. This may be attributed to a reduced content of porosities of the HPHT-SB-EP condition compared to the HT-SB and the HT-SB-EP conditions. The results confirm the higher strength values obtained from the tensile tests in the HPHT-SB-EP condition.

3.3. Surface morphology

Before the fatigue test, SEM analysis was conducted on specimen surfaces from the gripped end. Fig. 6 presents SEM observations of the surface morphology of the 1st and 2nd series specimens in each post-processing condition. The presence of surface discontinuities, even with decreased Ra, is displayed particularly on HT-SB specimens. The SB of the 2nd series (8 bar blasting) successfully reduced surface irregularities compared to the 1st series (refer to Fig. 6). Regarding the EP

Table 4
Mechanical properties measured on LPBF Ti6Al4V specimens.

1st series conditions	Properties			
	Young's modulus, E [GPa]	Yield strength, σ_y [MPa]	Ultimate tensile strength, σ_R [MPa]	Elongation at failure [%]
HT-SB	123 ± 2	900 ± 8	974 ± 11	11 ± 0
HT-SB-EP	113 ± 4	918 ± 2	979 ± 2	11 ± 1
HPHT-SB-EP	110 ± 4	959 ± 6	1029 ± 4	11 ± 0
2nd series conditions				
HT-SB	121 ± 8	884 ± 9	988 ± 17	8 ± 3
HT-SB-EP	116 ± 6	910 ± 16	1005 ± 14	10 ± 3
HPHT-SB-EP	112 ± 5	963 ± 12	1052 ± 13	14 ± 3

treatment, it effectively reduced surface roughness but did not completely affect the valleys of surface irregularities, with surface aberrations still visible in both 1st and 2nd series HT-SB-EP and HPHT-SB-EP specimens. In the 1st series, unmelted powder particles can be observed within deep surface irregularities of electropolished specimens, while in the 2nd series, these appear shallower and have a reduced size. Furthermore, the irregularities in the 2nd series have morphologies resembling the microstructure patterns, even though no etching is applied.

It is known that the valleys of surface topography play a crucial role in triggering the nucleation of cracks because they behave like sharp micro-notches acting as stress concentration sites at stress often exceeding twice the bulk stress [54–59]. Moreover, when comparing surfaces with different finishes, the most detrimental effect from a stress concentration point of view is given by a single micro-notch on a fairly flat surface rather than on a rough surface [54]. Successive adjacent micro-notches promote a lower degree of stress concentration on a rough surface than a single notch because stress is relaxed due to neighbouring notches [60]. Therefore, local defects contribute to the global stress field and can shift failure locations. In particular, fatigue initiation can be dominated by sharp and isolated defects, with stress concentration factors that depend on their location, depth, and morphology.

3.4. Fatigue test

Statistical elaborations of the fatigue test data for HT-SB, HT-SB-EP, and HPHT-SB-EP specimens from the 1st and 2nd series are presented in Fig. 7. Run-out specimens (marked with an arrow in Fig. 7) suggest that all conditions exhibit an asymptotic behaviour at low stress values. This is known as the fatigue limit at the knee or endurance limit (σ_e) of the S-N curve and is highlighted with a dashed line. Table 5 summarizes the determined fatigue properties: T_σ, k, σ_e, the maximum σ_{max} at which a run-out was observed, and the statistical fatigue limit ($\sigma_{max50\%}$) at 2×10^6 cycles estimated by extending the predicted S-N curve in the finite life region at the run-out limit through statistical elaboration. It is noteworthy that for each condition the maximum σ_{max} at which a run-out was observed is far higher than the $\sigma_{max50\%}$. The endurance limits for the 1st series are observed at about 300, 350, and 400 MPa, whereas for the 2nd series at about 375, 400, and 500 MPa. Therefore, the HPHT-SB-EP condition shows increases of σ_e of 14 % and 25 % compared to the HT-SB-EP condition in the 1st series and in the 2nd series respectively, while having an increase of 33 % compared with the HT-SB condition for both series (refer to Table 5). The analysis of the presented results in Fig. 7i and Table 5 indicates that the electropolished specimens in the 2nd series, especially the HPHT-SB-EP specimens, exhibit improved fatigue resistance compared to the 1st series. However, the scatter index values of the 2nd series are higher than those of the 1st series, even with an increase in the number of tested specimens for the 2nd series. This is due to the fact that reducing surface roughness increases fatigue sensitivity, which is accompanied by an increase in the scattering of results. The HT-SB condition displays the highest scatter in both fatigue campaigns, in line with the higher Ra and Rt values compared to the other conditions. It is important to consider that the obtained T_σ values should be interpreted in the context of no mechanical machining being applied to any specimen in any post-process state. In contrast to the other conditions, the slope of the HPHT-SB-EP curve decreased from 1st series to 2nd series, with an increase of the inverse slope factor of 1.5 times. Additionally, few of the failed specimens considered in the statistical elaboration are previous run-out specimens that were re-tested at higher loads in order to provide a more comprehensive analysis of the fatigue performance. For example, an HPHT-SB-EP specimen of the 1st series underwent three run-outs at 350, 450, and 500 MPa. It broke after 30,033 cycles under a stress amplitude of 600 MPa. Meanwhile, an HPHT-SB-EP specimen from the 2nd series underwent two run-out at 600 and 750 MPa. It broke after 3949 cycles under a stress amplitude of 800 MPa. The general observation of Fig. 7g-i and Table 5 shows that specimens of the 1st and 2nd series display similar trends, with the 2nd series data being shifted at higher loads for the same cycles to failure. Despite the scatter obtained, the HPHT-SB-EP appears to be the optimum condition, with a $\sigma_{max50\%}$ of 138 MPa for the 1st series and 362 MPa for the 2nd series.

3.5. Fractography

Fig. 8 illustrates SEM micrographs of the fracture surface of a HT-SB fatigue specimen from the 1st series. The micrographs serve as a representation of the nucleation and growth of fatigue cracks observed in all failed specimens, including: (a) the surface overview, (b) the crack initiation site, (c) the crack growth phase, (d) and the ductile failure region. Fatigue crack initiation occurred on one side of the cross-section and propagated towards the opposite side (as indicated by the red arrows in Fig. 8a) followed by sudden static failure with appreciable plastic deformation (as seen in Fig. 8d). The nucleation site can be observed at a long and shallow surface defect, highlighted in red in Fig. 8b.

Fig. 9 illustrates SEM micrographs of the fracture surfaces of fatigue specimens from both the 1st and 2nd series presenting, for each one, the surface overview (with red arrows indicating the crack propagation direction) and the crack initiation site. Table 6 presents average values of the surface irregularity dimension at fatigue crack initiation in terms of $\sqrt{area}$. Since fractography analysis did not reveal discernible differences in the fatigue crack growth phase and ductile failure region, a decision was made to report only Fig. 8c and 8d as representative of the morphological features observed in all specimens. In particular, fatigue crack growth can be observed as transgranular or intergranular, with the former generated when α lamellae have the main axes oriented parallel to the stress axis and the latter when α lamellae are oriented perpendicular to the load axis. Fractography analysis revealed that all specimens in the 1st series failed due to fatigue crack initiation at surface defects with irregular shapes, such as the ones highlighted in red in Fig. 9. Although the consecutive melting and solidification that happens between adjacent layers promotes material densification, some surface areas may not experience the same thermal history on the last track, resulting in the surface irregularities illustrated in Fig. 6. Reasons for such irregularities to occur depend upon LPBF process conditions and can be related, for instance, to melt pool instability, splashing of molten material, and balling phenomenon [61,62]. Additionally, since their size, shape, and location are different, it is clear how fatigue life data varies among individual specimens and not only among different post-processing conditions. This helps to explain why specimens in HT-SB-EP and HPHT-SB-EP conditions display a certain degree of scatter in fatigue results, despite having higher σ_e and lower average defect dimension at fatigue crack initiation than the ones in HT-SB condition (as seen in Table 6). Moreover, for the HT-SB and HT-SB-EP conditions the stress at the root of surface defects can be intensified by the potential

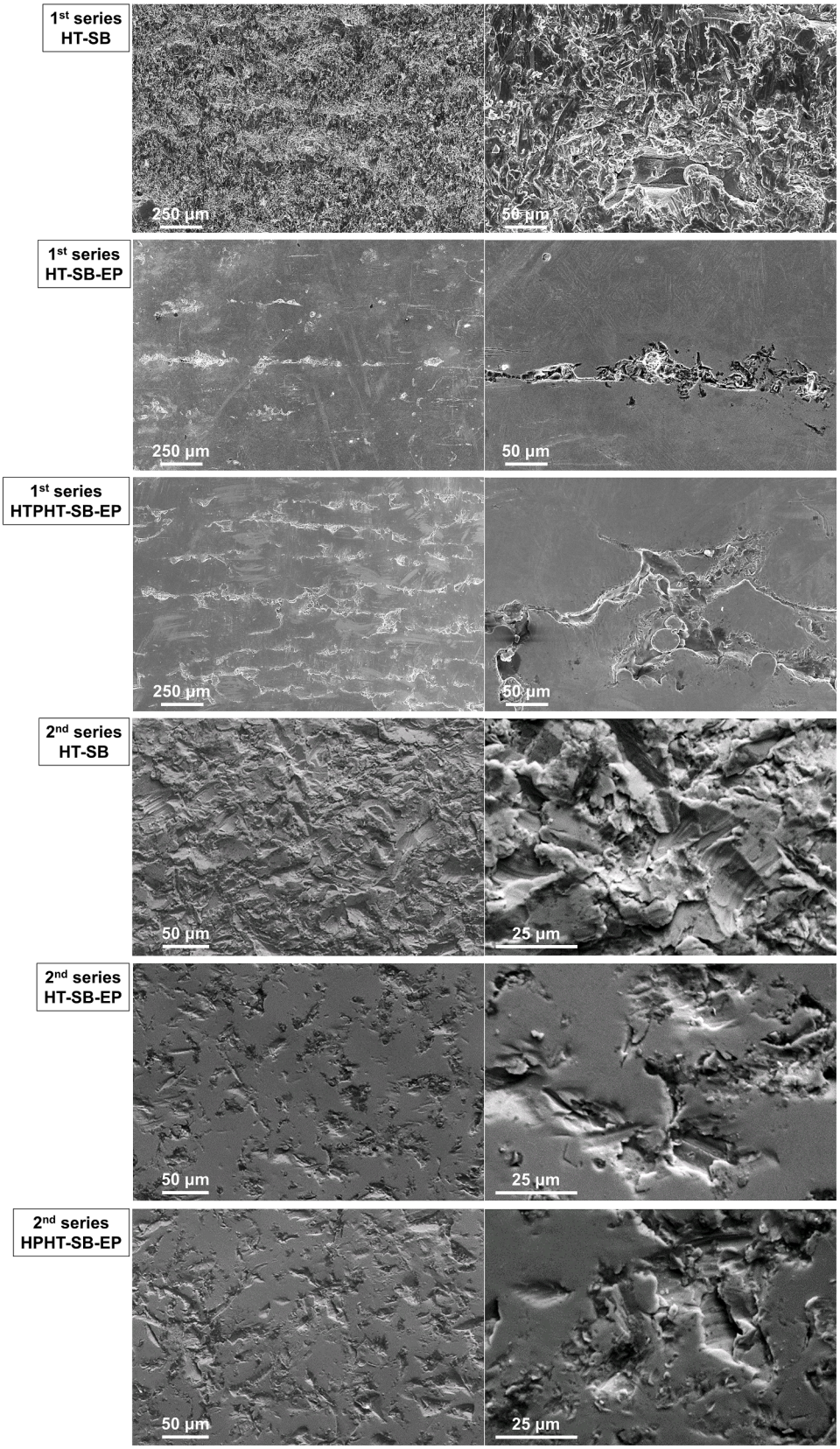

Fig. 6. SEM micrographs of the surface of HT-SB, HT-SB-EP, and HPHT-SB-EP specimens from 1st and 2nd series.

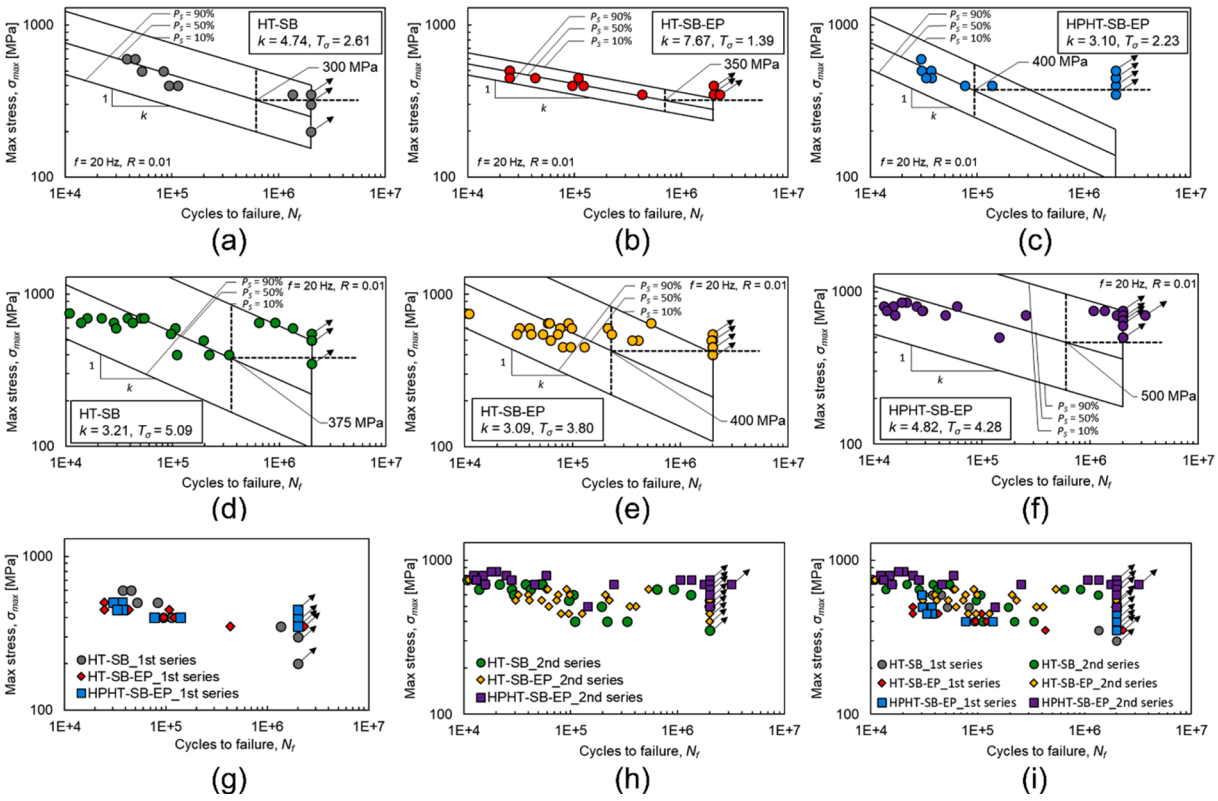

Fig. 7. Fatigue data for LPBF Ti6Al4V specimens (a–c) 1st series, (d–f) 2nd series, and (g–i) comparative representations.

Table 5
Fatigue properties of tested LPBF Ti6Al4V specimens.

Specimen series	Condition	Statistical fatigue limit, $\sigma_{50\%}$ [MPa]	Fatigue limit at knee, σ_e [MPa]	Maximum σ_{max} run-out [MPa]	T_σ	k
1st series	HT-SB	250	300	350	2.61	4.74
	HT-SB-EP	278	350	400	1.39	7.67
	HPHT-SB-EP	138	400	500	2.23	3.10
2nd series	HT-SB	220	375	550	5.09	3.21
	HT-SB-EP	212	400	550	3.80	3.09
	HPHT-SB-EP	362	500	750	4.28	4.82

interaction with internal defects, which makes it easier for cracks to nucleate form such locations. On the other hand, the HT-SB condition shows in both series the highest scattering due to larger surface defects. Regarding the 2nd series specimens, there were significant differences noted at the fatigue crack initiation sites, with a minor amount of relevant surface irregularities observed compared to the 1st series specimens (such as the HT-SB-EP and HPHT-SB-EP specimens reported in Fig. 9). This result confirms that the SB and EP treatments with the parameters of the 2nd series can be effective in reducing the influence of surface irregularities previously observed in the 1st series. In fact, defects with reduced dimensions were observed in the 2nd series as can be noted in Table 6. Since the defects responsible for fatigue crack nucleation are located at the surface of the specimens, the increase of sand-blasting pressure in the 2nd series was sufficient to reduce their size. Some defects with similar appearance and shape to the ones already detected in the 1st series were observed, particularly in HT-SB specimens (see Fig. 9). Only a few specimens exhibited a sub-surface initiation at depths of 135 ± 90 μm characterized by a faceted morphology, which influenced fatigue life scatter. The fracture in this area is quasi-cleavage, as it does not occur in a single well-defined crystalline plane, and the surface is composed of fewer smooth facets than in the case of a purely brittle fracture. In Ti6Al4V, the mechanism of quasi-cleavage is based on the formation of facets at the basal plane of the HCP α phase due to restricted slip on such plane. Slip activity in adjacent favourably oriented α grains transfers shear stress onto the non-favourably oriented α grain, introducing a tensile stress component that causes quasi-cleavage on the basal plane [63–65]. Considering the above, the sub-surface nucleation of fatigue cracks has to be considered as an additional factor influencing the fatigue life scatter of HT-SB-EP and HPHT-SB-EP.

As previously discussed, fatigue resistance improved in the 2nd series specimens with a decrease in surface roughness, regardless of the microstructure. Based on the observed crack initiation sites, the increase in scattering can be attributed to a reduced contribution of the shielding effect on stress concentration from surface irregularities and a heightened influence of the local microstructure. It is well known that variations in crystallographic orientation and microstructure at and near defects, such as surface roughness valleys, have a greater impact on fatigue initiation as the size of the defects decreases [66].

4. Conclusions

In conclusion, this research aimed to assess the impact of three distinct post-processing conditions (HT-SB, HT-SB-EP, and HPHT-SB-EP) on the fatigue behaviour of Ti6Al4V specimens produced via LPBF process. The investigation involved a thorough analysis of microstructures and mechanical properties, comprising two testing campaigns (1st and 2nd series) with increased SB pressure and reduced surface roughness for the latter. Key findings can be summarized as follows:

- Both the HT and the HPHT treatments successfully generated a macrostructure consisting of equiaxial parent β grains. The microstructure exhibited thin $\alpha + \beta$ lamellae organized in colonies within the grains, with α phase present at the parent β grain boundaries. No

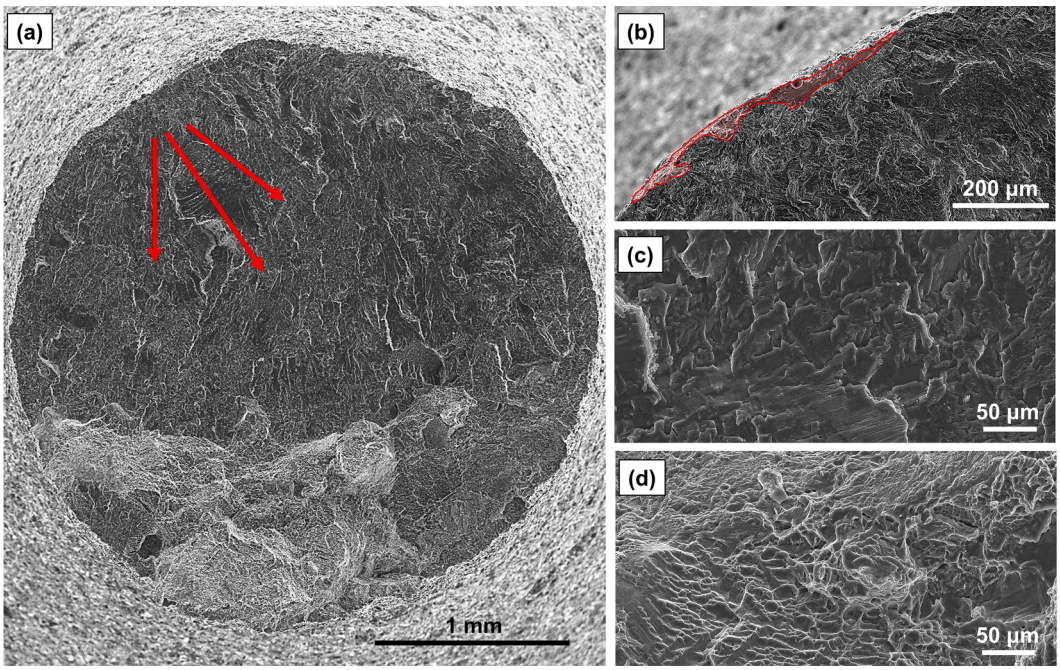

Fig. 8. SEM micrographs of the fracture surface of a HT-SB specimen from the 1st series.

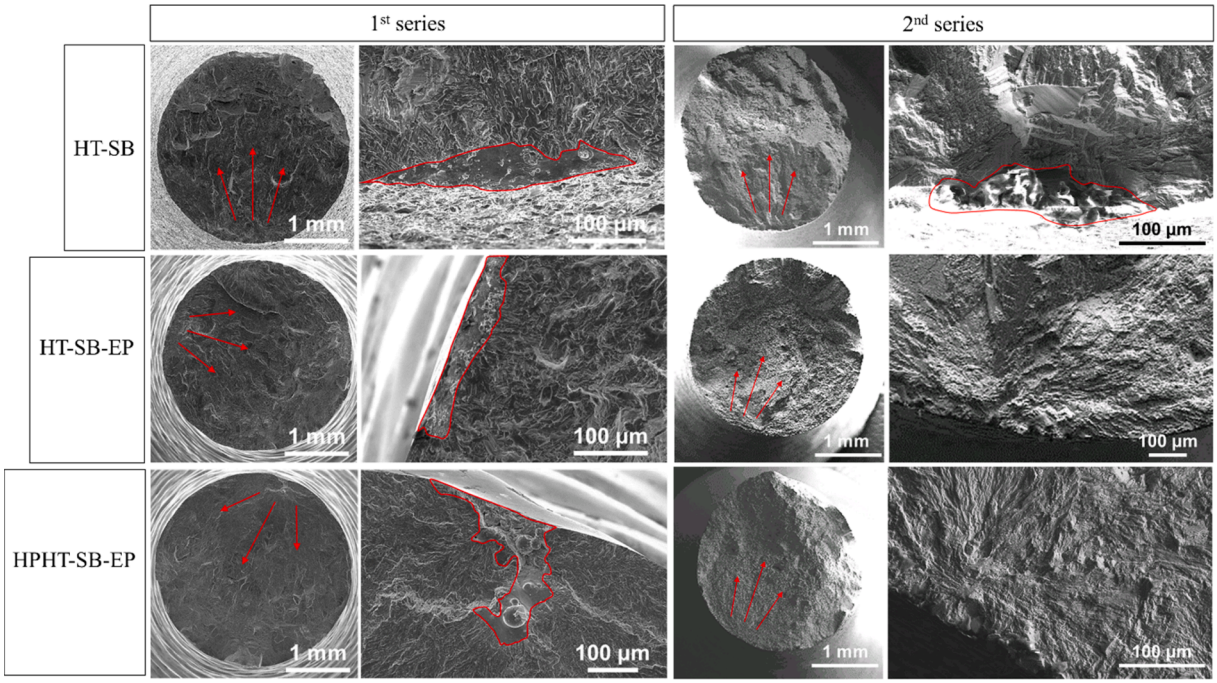

Fig. 9. SEM micrographs of the fracture surface of HT-SB, HT-SB-EP, and HPHT-SB-EP from 1st and 2nd series.

discernible influence on the microstructure was observed from the EP treatment.

- Tensile properties were consistent between the 1st and 2nd series, with the HPHT-SB-EP condition displaying values comparable to traditionally forged Ti6Al4V, showcasing a favourable balance between strength and ductility. The EP treatment exhibited a slight positive effect on both σ_y and σ_R when comparing specimens with the same thermal condition (HT-SB vs. HT-SB-EP). In the case of identical surface conditions (HT-SB-EP vs. HPHT-SB-EP), the application of pressure during heat treatment resulted in higher average values of σ_y, σ_R, and elongation at failure for the HPHT-SB-EP specimens.
- Microhardness results mirrored metallurgical characterization and tensile properties, showing a similar overall behaviour among post-processing conditions, with slightly higher hardness values for the HPHT-SB-EP condition.
- Surface morphology observations unveiled inherent surface discontinuities in all conditions due to the LPBF process. The 2nd series, with reduced surface roughness, effectively minimized surface irregularities. SB in the 2nd series successfully reduced surface aberrations, while the EP treatment, although beneficial, did not completely affect the valleys of surface irregularities in HT-SB-EP and HPHT-SB-EP specimens.

Table 6
Average surface irregularities dimension, $\sqrt{area}$, at fatigue crack initiation of 1st and 2nd series.

Specimen series	Condition	Average $\sqrt{area}$ of surface irregularities at fatigue crack initiation [μm]
1st series	HT-SB	174 ± 50
	HT-SB-EP	136 ± 51
	HPHT-SB-EP	139 ± 40
2nd series	HT-SB	124 ± 34
	HT-SB-EP	108 ± 56
	HPHT-SB-EP	98 ± 63

- Fatigue resistance of the 2nd series specimens, particularly in the HPHT-SB-EP condition, exhibited improvement compared to the 1st series. The HPHT-SB-EP condition showed a notable increase of $\sigma_{max50\%}$ from 138 MPa in the 1st series to 362 MPa in the 2nd series. Increased scatter in the 2nd series was attributed to reduced surface roughness and an augmented contribution of local surface defects and microstructure. The HT-SB condition displayed the highest scatter in both fatigue campaigns.
- Fractography analysis revealed that fatigue crack initiation in the 1st series occurred at surface defects due to stress concentration, whereas in the 2nd series surface defects with reduced dimensions were observed as initiation sites, with only a few specimens failing with initiation at sub-surface faceted regions and increased fatigue life.

In summary, the HPHT-SB-EP condition demonstrated superior mechanical and fatigue properties. The effectiveness of innovative post-processing techniques, specifically HPHT (simultaneous application of pressure and a heat treatment with quenching) and EP (dry electro-polishing) was underscored, especially when coupled with increased SB pressure to reduce surface roughness. The enhanced fatigue resistance of the HPHT-SB-EP condition is likely due to surface irregularities of reduced size and a potential diminished interaction between surface and internal defects.

CRediT authorship contribution statement

Omar Bologna: Writing – original draft, Investigation, Formal analysis, Data curation. **Silvia Cecchel:** Writing – review & editing, Visualization, Validation, Supervision, Resources, Methodology, Investigation, Funding acquisition, Formal analysis, Data curation, Conceptualization. **Giovanna Cornacchia:** Writing – review & editing, Visualization, Validation, Methodology, Investigation, Formal analysis, Data curation, Conceptualization. **Andrea Avanzini:** Writing – review & editing, Validation, Supervision, Methodology, Investigation, Formal analysis, Data curation, Conceptualization. **Raffaele Sepe:** Writing – review & editing, Investigation. **Filippo Berto:** Writing – review & editing, Supervision, Investigation, Formal analysis, Data curation. **Nima Razavi:** Writing – review & editing, Supervision, Methodology, Formal analysis, Data curation.

Declaration of competing interest

The authors declare that they have no known competing financial interests or personal relationships that could have appeared to influence the work reported in this paper.

Data availability

No data was used for the research described in the article.

Acknowledgements

The authors express their gratitude for the support provided by Streparava SpA. Additionally, they express their acknowledgement to the University of Brescia and the Norvegian University of Science and Technology of Trondheim. Within the framework of the *agreement for thesis research abroad* between these institutions, the author O.B. was able to conduct part of the research activities abroad.

References

[1] DebRoy T, Wei HL, Zuback JS, Mukherjee T, Elmer JW, Milewski JO, et al. Additive manufacturing of metallic components – process, structure and properties. Prog Mater Sci 2018;92:112–224. https://doi.org/10.1016/j.pmatsci.2017.10.001.
[2] Herzog D, Seyda V, Wycisk E, Emmelmann C. Additive manufacturing of metals. Acta Mater 2016;117:371–92. https://doi.org/10.1016/j.actamat.2016.07.019.
[3] Leal R, Barreiros FM, Alves L, Romeiro F, Vasco JC, Santos M, et al. Additive manufacturing tooling for the automotive industry. Int J Adv Manuf Technol 2017;92:1671–6. https://doi.org/10.1007/s00170-017-0239-8.
[4] Jankovics D, Barari A. Customization of automotive structural components using additive manufacturing and topology optimization. IFAC-PapersOnLine 2019;52:212–7. https://doi.org/10.1016/j.ifacol.2019.10.066.
[5] Helms H, Lambrecht UL. The potential contribution of light-weighting to reduce transport energy consumption. Int J Life Cycle Assess 2007;12:58–64.
[6] Kim HC, Wallington TJ. Life-cycle energy and greenhouse gas emission benefits of lightweighting in automobiles: review and harmonization. Environ Sci Tech 2013;47:6089–97. https://doi.org/10.1021/es3042115.
[7] Cecchel S. Materials and technologies for lightweighting of structural parts for automotive applications: a review. SAE Int J Mater Manuf 2021;14:5–14. https://doi.org/10.4271/05-14-01-0007.
[8] Sanaei N, Fatemi A. Defects in additive manufactured metals and their effect on fatigue performance: a state-of-the-art review. Prog Mater Sci 2021;117:100724. https://doi.org/10.1016/j.pmatsci.2020.100724.
[9] Bellini C, Berto F, Di Cocco V, Iacoviello F, Mocanu LP, Razavi J. Additive manufacturing processes for metals and effects of defects on mechanical strength: a review. Procedia Struct Integr 2021;33:498–508. https://doi.org/10.1016/j.prostr.2021.10.057.
[10] Lewandowski JJ, Seifi M. Metal additive manufacturing: a review of mechanical properties. Annu Rev Mat Res 2016;46:151–86. https://doi.org/10.1146/annurev-matsci-070115-032024.
[11] Yadollahi A, Shamsaei N. Additive manufacturing of fatigue resistant materials: challenges and opportunities. Int J Fatigue 2017;98:14–31. https://doi.org/10.1016/j.ijfatigue.2017.01.001.
[12] Yadroitsev I, Yadroitsava I, Plessis A Du, MacDonald E, editors. Fundamentals of Laser Powder Bed Fusion of Metals. 1st ed. Elsevier Ltd; 2021. doi: doi: 10.1016/C2020-0-01200-4.
[13] du Plessis A, Macdonald E. Hot isostatic pressing in metal additive manufacturing: X-ray tomography reveals details of pore closure. Addit Manuf 2020;34:101191. https://doi.org/10.1016/j.addma.2020.101191.
[14] Cecchel S, Ferrario D, Mega F, Cornacchia G. Numerical, mechanical, and metallurgical investigation of an innovative near net shape titanium selective laser melting engine component and comparison with the conventional forged one. Adv Eng Mater 2021;23:1–10. https://doi.org/10.1002/adem.202100036.
[15] Lütjering G, Williams JC. Titanium. 2nd ed. Springer Berlin, Heidelberg; 2007. doi: doi: 10.1007/978-3-540-73036-1.
[16] Schauerte O. Titanium in automotive production. Adv Eng Mater 2003;5:411–8. https://doi.org/10.1002/adem.200310094.
[17] Froes FH, Friedrich H, Kiese J, Bergoint D. Titanium in the family automobile: The cost challenge. Cost - Afford Titanium, Symp Dedic to Profr Harvey Flower 2004:159–66. doi: 10.1007/s11837-004-0144-0.
[18] Cecchel S, Ferrario D, Cornacchia G, Gelfi M. Development of heat treatments for selective laser melting Ti6Al4V alloy: effect on microstructure, mechanical properties, and corrosion resistance. Adv Eng Mater 2020;22:1–12. https://doi.org/10.1002/adem.202000359.
[19] Cecchel S, Mohammad Javad Razavi S, Mega F, Cornacchia G, Avanzini A, Battini D, et al. Fatigue testing and end of life investigation of a topology optimized connecting rod fabricated via selective laser melting. Int J Fatigue 2022;164:107134. https://doi.org/10.1016/j.ijfatigue.2022.107134.
[20] Pegues JW, Shao S, Shamsaei N, Sanaei N, Fatemi A, Warner DH, et al. Fatigue of additive manufactured Ti-6Al-4V, Part I: the effects of powder feedstock, manufacturing, and post-process conditions on the resulting microstructure and defects. Int J Fatigue 2020;132. https://doi.org/10.1016/j.ijfatigue.2019.105358.
[21] Kahlin M, Ansell H, Basu D, Kerwin A, Newton L, Smith B, et al. Improved fatigue strength of additively manufactured Ti6Al4V by surface post processing. Int J Fatigue 2020;134:105497. https://doi.org/10.1016/j.ijfatigue.2020.105497.
[22] Bhandari L, Gaur V. Different post-processing methods to improve fatigue properties of additively built Ti-6Al-4V alloy. Int J Fatigue 2023;176:107850. https://doi.org/10.1016/j.ijfatigue.2023.107850.
[23] Andrew Hills M, Scott Malcolm J, Mohamed Dhansay N, Hermann BT. High cycle fatigue strength of hot isostatically pressed and chemically etched laser powder bed fusion produced Ti-6Al-4V. Int J Fatigue 2023;175:107774. https://doi.org/10.1016/j.ijfatigue.2023.107774.

[24] Emanuelli L, Molinari A, Facchini L, Sbettega E, Carmignato S, Bandini M, et al. Effect of heat treatment temperature and turning residual stresses on the plain and notch fatigue strength of Ti-6Al-4V additively manufactured via laser powder bed fusion. Int J Fatigue 2022;162:107009. https://doi.org/10.1016/j.ijfatigue.2022.107009.

[25] Sun YY, Lu SL, Gulizia S, Oh CH, Fraser D, Leary M, et al. Fatigue performance of additively manufactured Ti-6Al-4V: surface condition vs. Internal Defects Jom 2020;72:1022–30. https://doi.org/10.1007/s11837-020-04025-7.

[26] Molaei R, Fatemi A, Sanaei N, Pegues J, Shamsaei N, Shao S, et al. Fatigue of additive manufactured Ti-6Al-4V, Part II: the relationship between microstructure, material cyclic properties, and component performance. Int J Fatigue 2020;132. https://doi.org/10.1016/j.ijfatigue.2019.105363.

[27] Liu S, Shin YC. Additive manufacturing of Ti6Al4V alloy: a review. Mater Des 2019;164:107552. https://doi.org/10.1016/j.matdes.2018.107552.

[28] Rao JH, Stanford N. A survey of fatigue properties from wrought and additively manufactured Ti-6Al-4V. Mater Lett 2021;283:128800. https://doi.org/10.1016/j.matlet.2020.128800.

[29] Acquesta A, Monetta T. The electropolishing of additively manufactured parts in titanium: state of the art. Adv Eng Mater 2021;23. https://doi.org/10.1002/adem.202100545.

[30] Soto M, Gutiérrez D. Innovation in electropolishing: Greater selectivity and definition with DryLyte dry electropolishing. DryLyte Technol 2019:1–3. https://imr.ie/wp-content/uploads/2021/03/a976fd_34eec0adbcdb45fea35c5288953a7097-1.pdf (accessed 21 February 2024).

[31] Simeunovic S, Jung C, Mory D, Seiler D, De WM. Investigating dry electro-chemical polishing of titanium structures novel polishing methods for the MedTech industry. Curr Dir Biomed Eng 2021;7:77–80. https://doi.org/10.1515/cdbme-2021-2020.

[32] Woo H, Kim J, Ryu J, Lee J, Lee S. Dry electropolishing of an additively manufactured spacer grid. Trans Korean Nucl Socit 2020:9–11 (https://www.kns.org/files/pre_paper/43/20S-287-우한길.pdf (accessed 21 February 2024)).

[33] Leuders S, Thöne M, Riemer A, Niendorf T, Tröster T, Richard HA, et al. On the mechanical behaviour of titanium alloy TiAl6V4 manufactured by selective laser melting: fatigue resistance and crack growth performance. Int J Fatigue 2013;48:300–7. https://doi.org/10.1016/j.ijfatigue.2012.11.011.

[34] Soundarapandiyan G, Khan R, Johnston C, Chen B, Fitzpatrick M. Effect of postprocessing thermal treatments on electron-beam powder bed–fused Ti6Al4V. Mater Des Process Commun 2021;3:1–8. https://doi.org/10.1002/mdp2.168.

[35] Tammas-Williams S, Withers PJ, Todd I, Prangnell PB. Porosity regrowth during heat treatment of hot isostatically pressed additively manufactured titanium components. Scr Mater 2016;122:72–6. https://doi.org/10.1016/j.scriptamat.2016.05.002.

[36] Cunningham R, Nicolas A, Madsen J, Fodran E, Anagnostou E, Sangid MD, et al. Analyzing the effects of powder and post-processing on porosity and properties of electron beam melted Ti-6Al-4V. Mater Res Lett 2017;5:516–25. https://doi.org/10.1080/21663831.2017.1340911.

[37] Ahlfors M. High pressure heat treatment of AM parts - Combining HIP and heat treatment. 30th ASM Heat Treat Soc Conf Expo Heat Treat 2019 - Ext Abstr 2019;2:11–7. doi: 10.31399/asm.cp.ht2019p0011.

[38] Rogers K, Slattery DSc K, Barnes J, Barnes T. The Advantage of Combining Hot Isostatic Pressing and Heat Treating Cycles in Additively Manufactured Components 2020:1–10. https://quintustechnologies.com/knowledge-center/the-advantage-of-combining-hot-isostatic-pressing-and-heat-treating-cycles-in-additively-manufactured-components/ (accessed 21 February 2024).

[39] Developments in Post Treatment Technologies n.d. https://quintustechnologies.com/knowledge-center/developments-in-post-treatment-technologies/ (accessed 15 April 2024).

[40] EOS. EOS Titanium Ti64 Grade 23 Material Data Sheet Metal Solutions 2023. https://www.eos.info/03_system-related-assets/material-related-contents/metal-materials-and-examples/metal-material-datasheet/titan/ti64/material_datasheet_eos_titanium_ti64_grade5_en_web.pdf (accessed 21 February 2024).

[41] Moran TP, Carrion PE, Lee S, Shamsaei N, Phan N, Warner DH. Hot isostatic pressing for fatigue critical additively manufactured Ti-6Al-4V. Materials (Basel) 2022;15:1–12. https://doi.org/10.3390/ma15062051.

[42] Benedetti M, Torresani E, Leoni M, Fontanari V, Bandini M, Pederzolli C, et al. The effect of post-sintering treatments on the fatigue and biological behavior of Ti-6Al-4V ELI parts made by selective laser melting. J Mech Behav Biomed Mater 2017;71:295–306. https://doi.org/10.1016/j.jmbbm.2017.03.024.

[43] ISO UNI EN 6892–1:2009, Metallic Materials–Tensile Testing–Part 1:Method of Test at Room Temperature. Geneva: International Organization for Standardization (ISO); 2009.

[44] ASTM E92-16, Standard Test Methods for Vickers Hardness and Knoop Hardness of Metallic Materials. West Conshohocken: ASTM International; 2016.

[45] ASTM E466-21 Standard Practice for Conducting Force Controlled Constant Amplitude Axial Fatigue Tests of Metallic Materials. ASTM International; 2021. doi: 10.1520/E0466-21.

[46] ASTM. Standard Practice for Statistical Analysis of Linear or Linearized Stress-Life (S-N) and Strain-Life (e-N) Fatigue Data 1. Annu B ASTM Stand 2012;i:1–7. doi: 10.1520/E0739-10R15.

[47] ISO 12107:2012 - Metallic materials — Fatigue testing — Statistical planning and analysis of data n.d. https://www.iso.org/standard/50242.html (accessed 21 February 2024).

[48] Gil Mur FX, Rodríguez D, Planell JA. Influence of tempering temperature and time on the α′-Ti-6A1-4V martensite. J Alloy Compd 1996;234:287–9. https://doi.org/10.1016/0925-8388(95)02057-8.

[49] Gil FJ, Ginebra MP, Manero JM, Planell JA. Formation of α-widmanstätten structure: effects of grain size and cooling rate on the widmanstätten morphologies and on the mechanical properties in Ti6Al4V alloy. J Alloy Compd 2001;329:142–52. https://doi.org/10.1016/S0925-8388(01)01571-7.

[50] Cecchel S, Montesano L, Cornacchia G. Wear and corrosion characterization of a Ti–6Al–4V component for automotive applications: forging versus selective laser melting technologies. Adv Eng Mater 2022;24:1–10. https://doi.org/10.1002/adem.202200082.

[51] Plöchl L, Manager BD, Ab QT, Gårdstam J, Manager AD, Ab QT, et al. Optimized HIP and Heat Treatment for Fatigue Strength of Additively Manufactured Ti6Al4V. accessed 21 February 2024 Quintus White Pap 2020:1–10. https://quintustechnologies.com/knowledge-center/optimized-hip-and-heat-treatment-for-fatigue-strength-of-additively-manufactured-ti6al4v/.

[52] Poondla N, Srivatsan TS, Patnaik A, Petraroli M. A study of the microstructure and hardness of two titanium alloys: commercially pure and Ti-6Al-4V. J Alloy Compd 2009;486:162–7. https://doi.org/10.1016/j.jallcom.2009.06.172.

[53] Torres Y, Sarria P, Gotor FJ, Gutiérrez E, Peon E, Beltrán AM, et al. Surface modification of Ti-6Al-4V alloys manufactured by selective laser melting: microstructural and tribo-mechanical characterization. Surf Coatings Technol 2018;348:31–40. https://doi.org/10.1016/j.surfcoat.2018.05.015.

[54] Gao H. Stress concentration at slightly undulating surfaces. J Mech Phys Solids 1991;39:443–58. https://doi.org/10.1016/0022-5096(91)90035-M.

[55] Taylor D, Clancy OM. The fatigue performance of machined surfaces. Fatigue Fract Eng Mater Struct 1991;14:329–36. https://doi.org/10.1111/j.1460-2695.1991.tb00662.x.

[56] Chan KS. Characterization and analysis of surface notches on Ti-alloy plates fabricated by additive manufacturing techniques. Surf Topogr Metrol Prop 2015;:3. https://doi.org/10.1088/2051-672X/3/4/044006.

[57] Chan KS, Koike M, Mason RL, Okabe T. Fatigue life of titanium alloys fabricated by additive layer manufacturing techniques for dental implants. Metall Mater Trans A 2013;44:1010–22. https://doi.org/10.1007/s11661-012-1470-4.

[58] du Plessis A, Beretta S. Killer notches: the effect of as-built surface roughness on fatigue failure in AlSi10Mg produced by laser powder bed fusion. Addit Manuf 2020;35:101424. https://doi.org/10.1016/j.addma.2020.101424.

[59] Vayssette B, Saintier N, Brugger C, El May M, Pessard E. Numerical modelling of surface roughness effect on the fatigue behavior of Ti-6Al-4V obtained by additive manufacturing. Int J Fatigue 2019;123:180–95. https://doi.org/10.1016/j.ijfatigue.2019.02.014.

[60] Murakami Y, Endo M. Effects of defects, inclusions and inhomogeneities on fatigue strength. Int J Fatigue 1994;16:163–82. https://doi.org/10.1016/0142-1123(94)90001-9.

[61] Qiu C, Panwisawas C, Ward M, Basoalto HC, Brooks JW, Attallah MM. On the role of melt flow into the surface structure and porosity development during selective laser melting. Acta Mater 2015;96:72–9. https://doi.org/10.1016/j.actamat.2015.06.004.

[62] Yuan W, Chen H, Cheng T, Wei Q. Effects of laser scanning speeds on different states of the molten pool during selective laser melting: simulation and experiment. Mater Des 2020;189:108542. https://doi.org/10.1016/j.matdes.2020.108542.

[63] Bridier F, Villechaise P, Mendez J. Slip and fatigue crack formation processes in an α/β titanium alloy in relation to crystallographic texture on different scales. Acta Mater 2008;56:3951–62. https://doi.org/10.1016/j.actamat.2008.04.036.

[64] Bantounas I, Dye D, Lindley TC. The role of microtexture on the faceted fracture morphology in Ti-6Al-4V subjected to high-cycle fatigue. Acta Mater 2010;58:3908–18. https://doi.org/10.1016/j.actamat.2010.03.036.

[65] Jha SK, Szczepanski CJ, Golden PJ, Porter WJ, John R. Characterization of fatigue crack-initiation facets in relation to lifetime variability in Ti-6Al-4V. Int J Fatigue 2012;42:248–57. https://doi.org/10.1016/j.ijfatigue.2011.11.017.

[66] Shamir M, Syed AK, Janik V, Biswal R, Zhang X. The role of microstructure and local crystallographic orientation near porosity defects on the high cycle fatigue life of an additive manufactured Ti-6Al-4V. Mater Charact 2020;169:110576. https://doi.org/10.1016/j.matchar.2020.110576.